Ausbildung großskaliger Wirbel in der Umgebung des Drehmomentenmaximums in der Taylor-Couette Strömung

Formation of large scale vortices in the torque maximum region in Taylor-Couette flow

Andreas Froitzheim[1], Rodrigo Ezeta[2] Sebastian Merbold[1], Christoph Egbers[1], Detlef Lohse[2], Chao Sun[2]

[1]Lehrstuhl Aerodynamik und Strömungslehre, Brandenburgisch Technische Universität Cottbus-Senftenberg, Siemens-Halske-Ring 14, 03046 Cottbus, Deutschland

[2]Physics of Fluids Group, MESA+ Institute and J.M. Burgers Centre for Fluid Dynamics, University of Twente, P.O. Box 217, 7500 AE Enschede, The Netherlands

Schlagworte: Taylor-Couette, Turbulenz, PIV, Taylor-Wirbel
Key words: Taylor-Couette, turbulence, PIV, Taylor vortices

Summary

We are investigating turbulent Taylor-Couette flow experimentally using PIV in horizontal planes at different cylinder heights. When both cylinders rotate slightly in counter direction a maximum appears in the angular momentum transport due to a formation of large scale vortices inside the gap. These vortices can survive also in the fully turbulent regime, where turbulent fluctuations were assumed to prevent structure formations. Therefore, we want to analyze the contribution of these vortices to the overall angular momentum flux and their strength in the classical turbulent and ultimate turbulent regime at varying rotation rates. We try to get a better understanding of the importance of the Taylor vortices with an increasing level of turbulence.

Introduction

The flow between concentric rotating cylinders – namely Taylor-Couette flow – is a famous reserve model for rotating flows in fluid mechanics with various applications as journal bearings, turbines or compressors. Its geometry is defined by the radius ratio $\eta = r_1/r_2$ and the aspect ratio $\Gamma = L/d$ with the cylinder length L, the cylinder radii r_1 and r_2 for the inner and outer one respectively and the gap width $d = r_2 - r_1$ (see figure 1 left). To describe the cylinder speeds, we use the ratio of angular velocities $\mu = \omega_2/\omega_1$ and the shear Reynolds number $Re_S = 2 r_1 r_2 d |\omega_2 - \omega_1| / (v(r_1 + r_2))$ (Dubrulle et al. 2005). v represents the kinematic viscosity.

The transport of angular momentum in TC flows can by quantified by the quasi Nusselt number Nu_ω which is directly connected to torque T acting on the cylinder walls according to Eckhardt et al (2007b). At a constant shear rate inside the flow this torque exhibits a maximum in the low counter rotating regime [(Brauckmann & Eckhardt (2013a,b), Merbold et al. (2013), Ostilla et al. (2013)]. In the flow field this maximum is accompanied with a flattening of the angular velocity profile and a strengthening or rather forming of large scale vortices [Ostilla-Mónico et al. (2013, 2014a,b), Van der Veen et al. (2016), Van Gils et al. (2012)]. These vortices do survive, at least for counter rotation, also in the fully turbulent regime at the order of $Re = 10^6$ and different vortex states can exist contradictory to Kolmogorovs idea of turbulence

[Huisman et al. (2014), Van der Veen et al. (2012)]. In addition to the forming of large scale vortices an axial oscillation of these vortices was identified in the torque maximum region [Merbold et al. (2014)]. In summary, it is obvious that turbulent Taylor vortices play a prominent role for the angular momentum transport in TC flow even at high Reynolds numbers. Therefore we want to analyze their influence on the flow field in general and their contribution to the overall angular momentum flux specifically. This paper focuses on the measurement procedure and the calibration process.

Experimental Setup and Measurement procedure

To investigate turbulent Taylor vortices we performed PIV measurements in horizontal planes at 23 different cylinder heights at $\mu=0$, the torque maximum rotation rate ($\mu_{max}(\eta=0.714)=-0.36$) and for stronger counter rotation ($\mu=-0.71$). The experiments were carried out inside the Boiling-Turbulent-Taylor-Couette experiment (BTTC) of the University of Twente within the EuHIT-program.
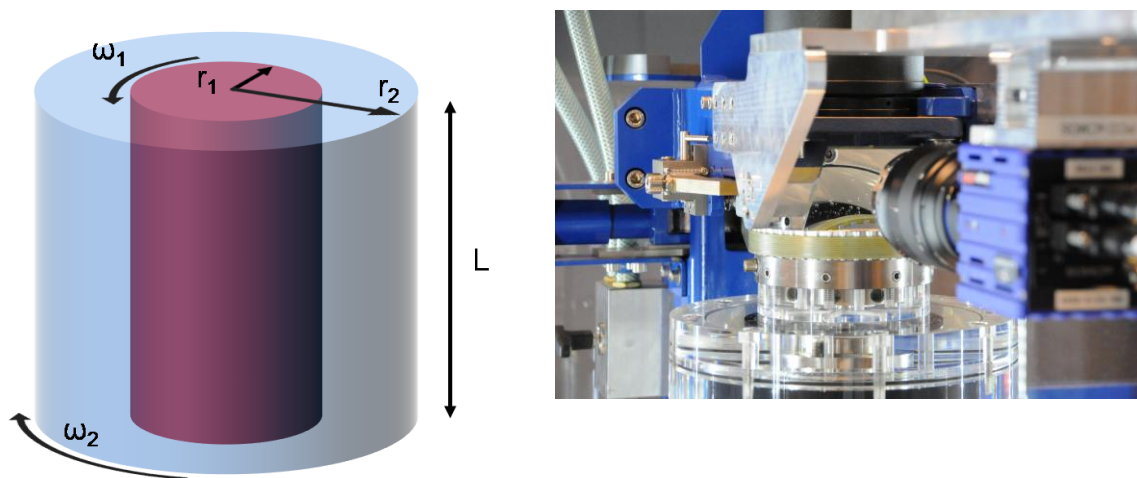

Fig. 1: Sketch of the Taylor-Couette geometry (left) and image of the PIV-Camera setup with a mirror at 45° above the transparent top plate of the Boiling-Turbulent-Taylor-Couette experiment at the University of Twente (right).

We will focus on the most important features of the BTTC facility, further details can be found in Huisman et al. (2015). The radii of the cylinders are r_1=75 mm and r_2=105 mm with a length of L=549 mm leading to a radius ratio of η=0.714, an aspect ratio of Γ=18.3 and a gap with of d=30 mm. The outer cylinder (OC) and the top plate are made of PMMA to enable optical access to the flow. Both endplates are fixed to the outer cylinder and rotate at the same speed. The inner cylinder (IC) is made of copper, chrome plated and splitted into three segments to possibly measure the torque in the middle segment of length L_{mid}=489 mm. Further, the IC consists of cooling channels to actively control the fluid temperature and three PT100 temperature sensors at heights 0.22 L, 0.49 L and 0.76 L. Both cylinders are driven by servomotors and can reach f_1=±20 Hz and f_2=±10 Hz respectively. As working fluid distilled water is used with a kinematic viscosity of ν=1.004·10^{-6} m²/s at 20°C and fluorescent PMMA-Rhodamine B-particles are added as tracers with a mean diameter in the range of 1-20 μm. A dual-cavity EverGreen -Laser (532 nm) is mounted on a traverse creating a 2 mm thick light sheet in the radial-azimuthal plane scanning in a range of ±44 mm around mid height with a step size of 4 mm. The scattered light of the particles is captured using a mirror at 45° above the transparent top plate with a sCMOS camera with 2560 x 2160 px (see figure 1 right). The camera is further equipped with a Zeiss Makro Planar objective and a band pass filter for the wave length of the used laser. Therefore, only the fluorescent light of the tracer particles is captured within the camera and reflections of the cylinder walls are suppressed.

To investigate different flow states the cylinders were accelerated to their final speed following a waiting time of about 10 minutes to reach a stable flow state. The measurement itself consists of 1500 double images recorded at 15 Hz at each axial position. Experiments and post-processing were done with the software Davis from LaVision. To calculate velocity fields based on double images a final interrogation area size with 24 x 24 pixels and 50% overlap was used reaching a spatial resolution of $2.53 \cdot 10^{-4}$ m - $3.10 \cdot 10^{-4}$ m depending on the measurement height. In total all investigated flow states are summarized in table 1. Within this paper we will only focus on the one with $Re_S = 9.3 \cdot 10^9$ and $\mu = 0$:

Re_S	$9.3 \cdot 10^3$	$3.0 \cdot 10^4$	$6.7 \cdot 10^4$	$9.5 \cdot 10^4$	$2.1 \cdot 10^5$	$3.5 \cdot 10^5$
μ	*0* -0.15 -0.36	-0.36	-0.36	-0.36	0 -0.36 -0.71	0

Tab. 1: Investigated parameter space in terms of the shear Reynolds number Re_S and the rotation ratio μ. The underlined flow state is the one presented within this paper.

Calibration

A regular calibration using a calibration target was not applicable in this study, as the placement of this target inside the cylinder gap would require dismantling the top plate of the experiment. Due to the complexity of the experiment, the cylinder position would change between the calibration itself and the experimental run after resembling the facility again. Therefore, the PIV algorithm is performed on the double images in image coordinates x_{image} (units in px) resulting in image velocities u_{image} (units in px-displacement) and afterwards a transformation into real coordinates x_{real} and velocities u_{real} (units in m and m/s) is performed. The following method is based on a circle fit according to Gander et al. (1994). At first, we determine the location of the inner and outer cylinder in image coordinates. As we used a band pass filter during the measurements to reduce reflections on the cylinder walls, especially the inner cylinder is only slightly visible on the time averaged image. This problem can be avoided by using the standard deviation of the image sequence (see figure 2). However, we already calculated the velocity field and thus, we can also use the minimal and maximal velocity value at each x-position of the image to identify the location of both cylinders.
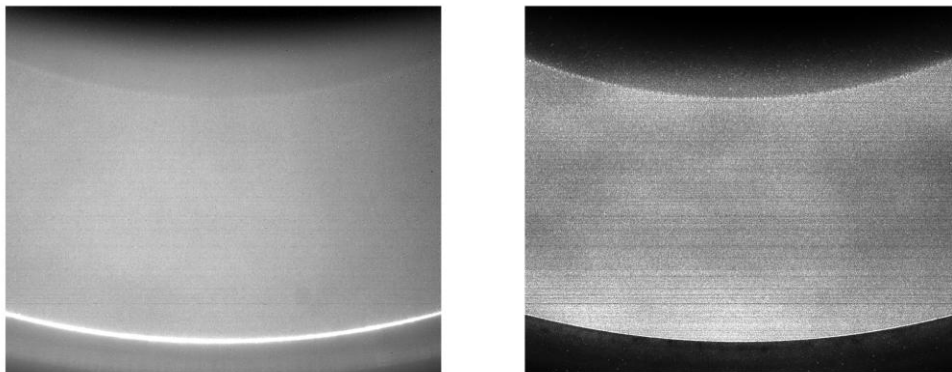

Fig. 2: Mean (left) and standard deviation (right) of the light intensity values of 1500 particle images at z-L/2=44 mm.

In the next step, concentric circles are fitted through the IC and OC points. As introduction, we will start with fitting only a single circle to the points x with a total number of points i=1:m. Let $g=(c_1,c_2,r)^T$ be the unknown center coordinates and radius of the circle and

$$d_i = \|c - x_i\|_2 - r \tag{1}$$

the distance of each point to the center. Then, we have to solve a nonlinear least square problem by minimizing the squared distances:

$$\sum_{i=1}^{m} d_i(\mathbf{g})^2 = \min \tag{2}$$

An iterative solution can be calculated by using a Taylor series around the solution $\hat{\mathbf{g}}$ with a correction vector $\mathbf{h}$:

$$\mathbf{d}(\hat{\mathbf{g}}+\mathbf{h}) \cong \mathbf{d}(\hat{\mathbf{g}}) + J(\hat{\mathbf{g}})\mathbf{h} \approx 0 \quad \rightarrow \quad J(\hat{\mathbf{g}})\mathbf{h} = -\mathbf{d}(\hat{\mathbf{g}}) \tag{3}$$

J represents the Jacobian and is calculated as

$$J = \begin{bmatrix} \dfrac{c_1 - x_{11}}{\|\mathbf{c} - \mathbf{x}_1\|_2} & \dfrac{c_2 - x_{12}}{\|\mathbf{c} - \mathbf{x}_1\|_2} & -1 \\ \vdots & \vdots & \vdots \\ \dfrac{c_1 - x_{m1}}{\|\mathbf{c} - \mathbf{x}_m\|_2} & \dfrac{c_2 - x_{m2}}{\|\mathbf{c} - \mathbf{x}_m\|_2} & -1 \end{bmatrix} = \begin{bmatrix} J^i & -1 \end{bmatrix} \tag{4}$$

The Iteration persists of solving equation 3 and then updating the approximation $\hat{\mathbf{g}}=\hat{\mathbf{g}}+\mathbf{h}$ according to the Gauss-Newton method. This algorithm can be extended to a fitting procedure of two concentric circles with the solution vector $g^{conc} = (c_1, c_2, r_{IZ}, r_{OZ})^T$, when the Jacobian and the function $\mathbf{d}$ are adapted:

$$J^{conc}(\mathbf{g}^{conc}) = \begin{bmatrix} J_{IZ}^i & -1 & 0 \\ J_{OZ}^i & 0 & -1 \end{bmatrix} \qquad \mathbf{d}(\mathbf{g}^{conc}) = \begin{bmatrix} \mathbf{d}(\mathbf{g}(c_1, c_2, r_{IZ})) \\ \mathbf{d}(\mathbf{g}(c_1, c_2, r_{OZ})) \end{bmatrix} \tag{5}$$
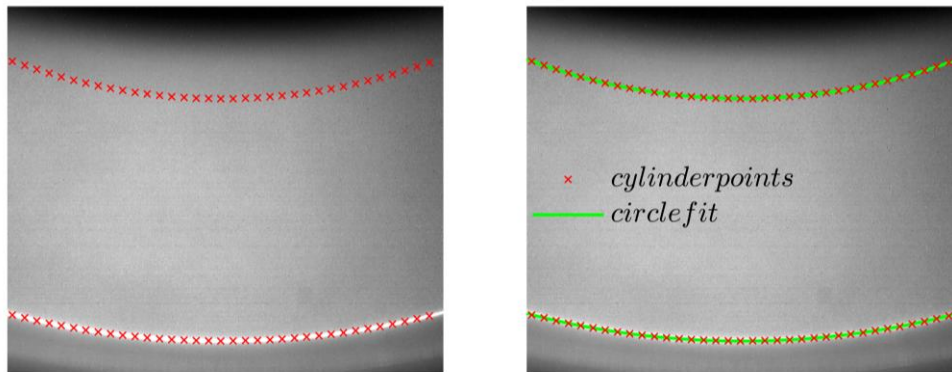
The result is depicted in figure 3.

Fig. 3: Mean of the light intensity values of 1500 particle images and image points coinciding with the location of the cylinder walls (red crosses). The green lines represent the best fit of concentric circles through the cylinder points. Height of horizontal plane: z-L/2=44 mm.

The determined IC and OC points are correctly located on the areas of high intensity, where the cylinders are displayed. The fitted concentric circles again reproduce these points. The ratio of fitted inner and outer cylinder radius is $r_{IZ}/r_{OZ}=0.715$ very close to the real radius ratio of $\eta=0.714$. If we assume to have a similarity transformation between the image and the real world, which is valid as we used a tele photo lens, the transformation from the image coordinates and velocities to the real ones is given by

$$\mathbf{x}_{real} = \begin{bmatrix} \dfrac{r_2 - r_1}{r_{OZ} - r_{IZ}} & 0 \\ 0 & \dfrac{r_2 - r_1}{r_{OZ} - r_{IZ}} \end{bmatrix} \left(\mathbf{x}_{image}^T - \mathbf{c}^T \right) \qquad \mathbf{u}_{real} = \begin{bmatrix} \dfrac{r_2 - r_1}{r_{OZ} - r_{IZ}} & 0 \\ 0 & \dfrac{r_2 - r_1}{r_{OZ} - r_{IZ}} \end{bmatrix} \dfrac{\mathbf{u}_{image}^T}{dt} \tag{6}$$

with dt representing the time between the double images. It has to be noticed that this calibration process is needed for each height position. The result for z=44 mm about mid height is depicted in figure 4:
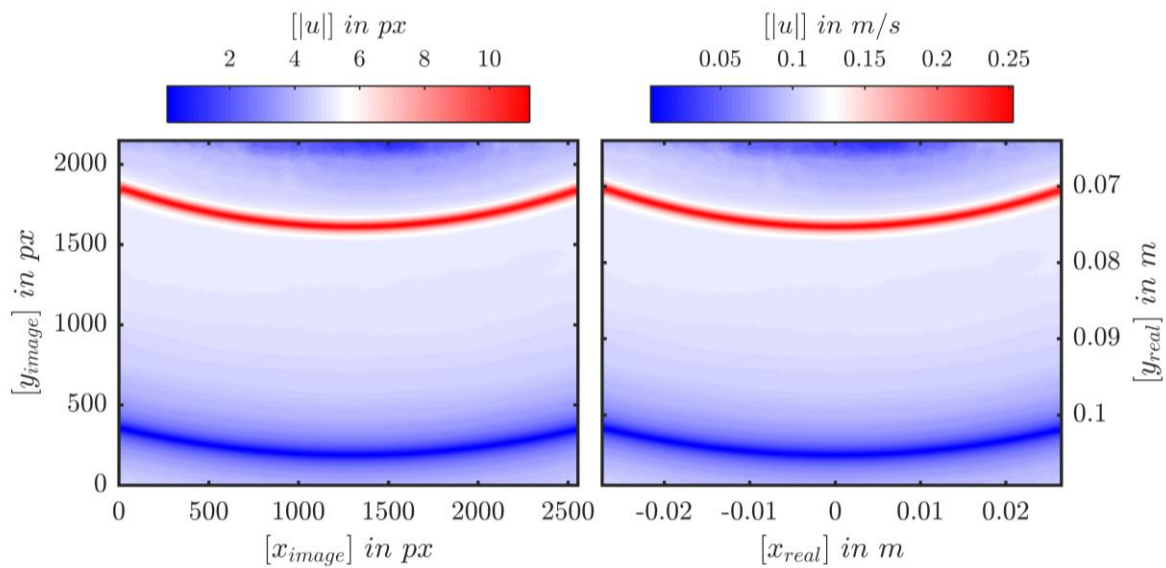

Fig. 4: Velocity value at horizontal plane height z-L/2=44 mm in terms of image and real coordinates.

Axial dependent velocity field

Within this paper we constrain the result evaluation to the flow state of $Re_S=9.3 \cdot 10^3$ and µ=0. In figure 5, the radial and azimuthal velocity components are depicted in terms of its average and standard deviation across time and the azimuthal coordinate direction as function of the axial and radial location. The radial coordinate and the azimuthal velocity are mapped to an interval between 0 and 1 using the transformation ř=(r-r_1)/(r_2-r_1) and u_φ=(u-$u_{\varphi,2}$)/($u_{\varphi,1}$-$u_{\varphi,2}$) respectively. The axial coordinate is centered around mid gap and normalized with the gap width d. The radial velocity component and the standard deviations are related to the shear velocity $ũ_r=u_r/u_s$ and $σ̃=σ/u_s$ with $u_s=(Re_S v)/d$:
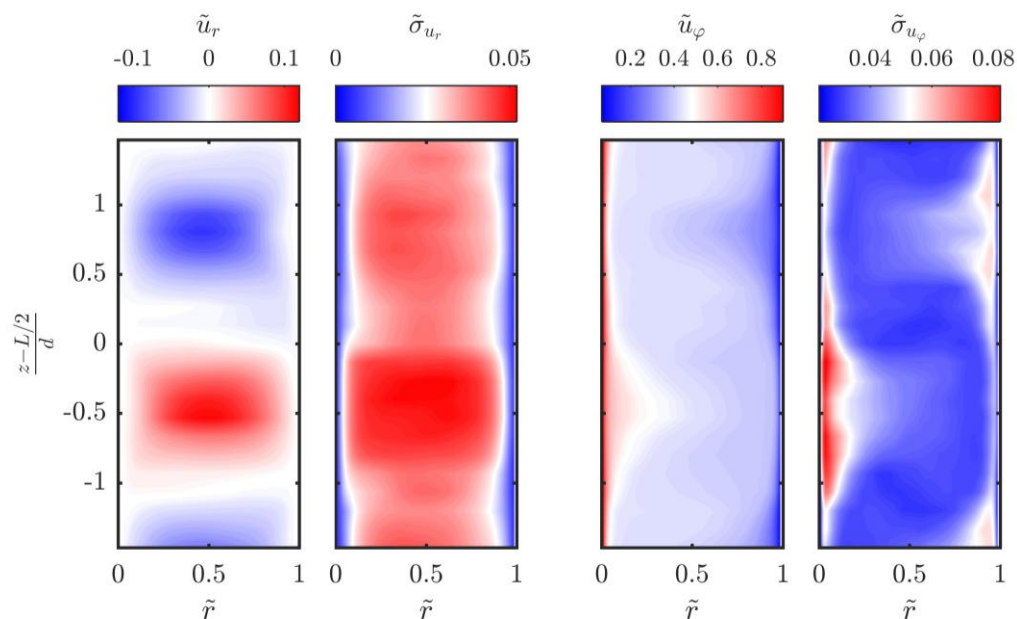

Fig. 5: Contour plots of mean and standard deviation of the radial and azimuthal velocity components across time and the azimuthal coordinate direction for $Re_S=9.3 \cdot 10^4$ and µ=0. Each contour plot consists of 23 height measurements separated by 4 mm in the axial coordinate direction.

The radial velocity component shows clearly large scale vortices with an inflow region transporting fluid from the outer to the inner cylinder and an outflow region with the reverse orientation. We defined the radial velocity component to be positive in the outflow region. Correspondingly, azimuthal velocity is transport in these regions strongly in wall normal direction indicating an additional convective momentum transport. The standard deviation of the radial velocity component is zero at the cylinder walls and exhibits a maximum in the center of the gap. Further, the maximum value is larger in the outflow than in the inflow region. The standard deviation of the azimuthal velocity component is low in the center of the gap and increases strongly especially near the inner cylinder in the outflow region and near the outer cylinder in the inflow region. To illustrate the differences between the prominent vortex regions, namely inflow, outflow and core region, we plotted these radial profiles in figure 6 together with the axial averaged profile. This average is restricted to the axial extension of one vortex pair instead of using the whole measurement domain:
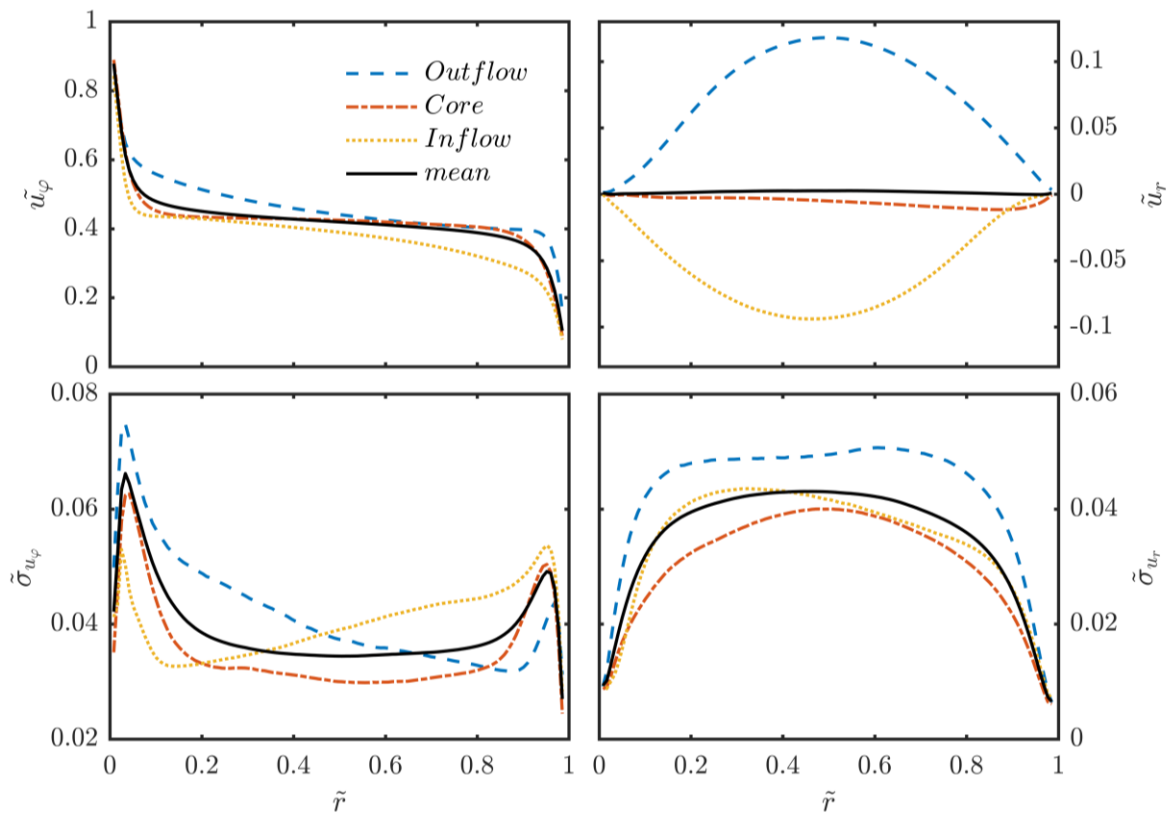

Fig. 6: Radial profiles of mean and standard deviation of the radial and azimuthal velocity component across time and the azimuthal coordinate for $Re_S=9.3\cdot10^4$ and $\mu=0$.

In regions, where fluid is transport away from the wall, the profile of angular velocity is flattened near the wall and in the opposite case the near wall profile becomes steeper in comparison to the averaged profile. Further, the angular velocity profile coinciding with the vortex core follows quite close the averaged one. The radial profiles are distributed around the zero line with a large amount in the center of the gap and opposite sign in the in- and outflow region and the profile for the core region and the averaged one are close to zero all over the gap. The standard deviation of the angular velocity shows in the averaged and core profile a large peak near the inner cylinder and a smaller peak near the outer cylinder and a low constant value in between. In the outflow region, the inner peak is enhanced, the outer one reduced and in the center, the value decreases with increasing ř. Again the contradictory behavior is visible in the inflow region. Lastly the profiles of the standard deviation of the radial velocity component have approximately all the same shape with a plateau in the center of the gap decreasing to zero in the near wall region. The outflow exhibits the largest amount in the gap. Similar results have also been found by Ostilla-Mónico et al. (2014b) for the same radius ratio and by Van der Veen et al. (2016) for η=0.5. Therefore we are confident to investi-

gate in the near future the axial dependence of the flow in the fully turbulent regime at high shear Reynolds numbers in the region of the torque maximum, where dominant Taylor vortices exist inside the gap. This will lead us to the quantification of the vortex contribution to the overall angular momentum flux.

Acknowledgements

Literature

Andereck C.D., Liu S.S., Swinney H.L., 1986: "Flow regimes in a circular Couette system with independently rotating cylinders", J. Fluid Mech. 164:155–83

Brauckmann, H.J. and Eckhardt, B., 2013a: "Direct numerical simulations of local and global torque in Taylor Couette flow up to Re=30000", J. Fluid Mech., 718:398-427

Brauckmann, H. J. and Eckhardt, B., 2013b: "Intermittent boundary layers and torque maxima in Taylor-Couette flow", Phys. Rev. E 87, 033004

Dubrulle, B., Dauchot, O., Daviaud, F., Longaretti, P.-Y., Richard, D. and Zahn, J.-P., 2005: "Stability and turbulent transport in Taylor–Couette flow from analysis of experimental data", Phys. Fluids 17, 095103

Eckhardt, B., Grossmann, S. and Lohse, D., 2007a: "Fluxes and energy dissipation in thermal convection and shear flows", Europhys. Lett. 78, 24001

Eckhardt, B., Grossmann, S., Lohse, D.,2007b: "Torque scaling in turbulent Taylor-Couette flow between independently rotating cylinders", J. Fluid Mech. 581, 221

Gander, W., Golub, G.H.,.Strebel, R.,1994:."Least-square fitting of circles and ellipses", BIT, (43):558-578

Huisman, S.G., van der Veen, R.C.A., Bruggert, G.W.H., Lohse, D., Sun, C., 2015: "The boiling Twente Taylor-Couette (BTTC) facility", Rev. Sci. Instrum., 86, 065108

Huisman, S.G., Roeland, C.A., van der Veen, Sun, C., Lohse, D.,2014: "Multiple states in highly turbulent Taylor-Couette flow", Nature Com

Merbold, S., Brauckmann, H.J., Egbers, Ch.,2013: "Torque measurements and numerical determination in differentially rotating wide gap Taylor-Couette flow", Phys. Rev. E 87, 023014

Merbold, S., Froitzheim, A., Egbers, Ch.,2014: „Flow pattern and angular motion transport in a wide gap Taylor-Couette flow", TU Dresden, Strömungstechnische Tagung 2014, Schriftenreihe aus dem Institut für Strömungsmechanik Band 10, ISBN 978-3-944331-78-2

Ostilla, R., Stevens, R.J.A.M., Grossmann, S., Verzicco, R. and Lohse, D.,2013: "Optimal Taylor-Couette flow: direct numerical simulations", J. Fluid Mech., 719: 14-46

Ostilla-Mónico, R., Huisman, S.G., Janninik, T.J.G., van Gils, D.P.M., Verzicco, R. et al.,2014a: "Optimal Taylor-Couette flow: radius ratio dependence", J. Fluid Mech. 747:1-29

Ostilla-Mónico, R., van der Poel, E.P., Verzicco, R., Grossmann, S., Lohse, D.,2014b: "Exploring the phase diagram of fully turbulent Taylor-Couette flow", J. Fluid Mech. 761:1–26

Poaletti, M. S. and Lathrop, D. P.,2011: "Angular Momentum Transport in Turbulent Flow between Independently Rotating Cylinders", Phys. Rev. Lett. 106, 024501

Van der Veen, R.C.A., Huisman, S.G., Merbold, S., Harlander, U., Egbers, Ch., Sun, C. and Lohse, D.,2016: "Taylor-Couette turbulence at radius ratio η=0.5: scaling, flow structures and plumes", J. Fluid Mech., 799: 334-351

Van der Veen, R.C.A., Huisman, S.G., Dung, O.-Y., Tang, H.L., Sun, C. and Lohse, D.,2012: "Exploring the phase space of multiple states in highly turbulent Taylor-Couette flow", Phys. Rev. Fluids 1, 024401, 2016 Van Gils, D. P. M., Huisman, S., Grossmann, S., Sun, C. and Lohse, D., Optimal Taylor-Couette turbulence, J. Fluid Mech. 706, 118

Van Gils, D. P. M., Huisman, S., Grossmann, S., Sun, C. and Lohse, D.,2012: "Optimal Taylor-Couette turbulence", J. Fluid Mech. 706, 118